Real-time synchronous imaging of electromechanical resonator mode and equilibrium profiles

Y. Linzon,[1,*] S. Krylov,[2] B. Ilic,[3] D. R. Southworth,[3] R. A. Barton,[1] B. R. Cipriany,[4] J. D. Cross,[1] J. M. Parpia,[5] and H. G. Craighead[1]

[1]School of Applied and Engineering Physics, Cornell University, Ithaca, New York 14853, USA

[2]School of Mechanical Engineering, Faculty of Engineering, Tel Aviv University, Tel Aviv 69978, Israel

[3]Center for Materials Research, Cornell University, Ithaca, New York 14853, USA

[4]School of Electrical and Computer Engineering, Cornell University, Ithaca, New York 14853, USA

[5]Department of Physics, Cornell University, Ithaca, New York 14853, USA

*Corresponding author: yoav.linzon@cornell.edu

Received May 25, 2010; accepted June 21, 2010;
posted July 9, 2010 (Doc. ID 128871); published July 30, 2010

Interferometric imaging of normal mode dynamics in electromechanical resonators, oscillating in the rf regime, is demonstrated by synchronous imaging with a pulsed nanosecond laser. Profiles of mechanical modes in suspended thin film structures and their equilibrium profiles are measured through all-optical Fabry–Perot reflectance fits to the temporal traces. As a proof of principle, the mode patterns of a microdrum silicon resonator are visualized, and the extracted vibration modes and equilibrium profile show good agreement with numerical estimations.

OCIS codes: 120.4880, 230.4685, 130.1750, 180.3170, 120.3180, 310.6845.

Owing to the rapid advances in fabrication technologies, micro- and nano-electromechanical system (MEMS and NEMS) resonators offer increasingly high mechanical frequencies of operation ranging from several to thousands of megahertz, and correspondingly high-quality factors [1,2]. These characteristics make them candidates for many applications, such as sensitive resonant sensors, filters, and timing devices [3]. In both MEMS and NEMS resonators, visualization of actuated vibration modes and equilibrium profiles provides important device characterization [4–13].

Scanning electron [4] and atomic force [5,6] microscopes offer unrivaled spatial resolutions in NEMS structure imaging. However, these tools cannot yield subcycle time-resolved images during *in situ* motion at rf. In the realm of optical characterization, several MEMS/NEMS visualization techniques are available [7–13], such as scanning interferometry of the Michelson [7,8], Mach–Zehnder [9], and heterodyne [10,11] types, as well as stroboscopic microscopy [8,12] and laser Doppler vibrometry [13]. Spatio-temporal characterization is usually based on scanning, and thus a common practical caveat is the requirement to use slow translation stages and complex data analysis algorithms, sacrificing acquisition times for high spatial resolutions and amplitude sensitivities.

In this Letter, we demonstrate real-time synchronous imaging of electromechanical mode patterns and profiles. This is realized by directly pulsing a nanosecond wide-field imaging laser synchronized with electrical drive. Temporal resolutions are attained by sweeping the phase difference between the drive and imaging beam signals.

Figure 1 illustrates our setup. The resonator resides in a vacuum chamber (4×10^{-2} Torr) with a front optical window and back electrical feedthrough. In the frequency domain scan (FDS) arm [Fig. 1(a)], the resonator is electrostatically driven by a swept rf network analyzer. The drive signal is amplified and subsequently dc-biased through an rf bias tee to maximize the mechanical amplitude and the associated interference depths of the reflected optical waves. A cw laser diode ($\lambda_0 =$ 633 nm) is focused by a long working distance objective lens (×20) onto the resonator, the substrate under which is reflective [14]. A polarizing beam splitter (PBS) collects and focuses the backreflected beam onto a low-noise sensitive detector. This closes a return loop with the analyzer. In the analyzer, the rf modulated signal is filtered and the spectral response is measured. This corresponds to the Fabry–Perot interferences matching each drive frequency. To avoid laser-induced artifacts that are not purely mechanical [3,15], minimum spot fluences (<0.2 mW/μm^2) are used. This arm is useful for

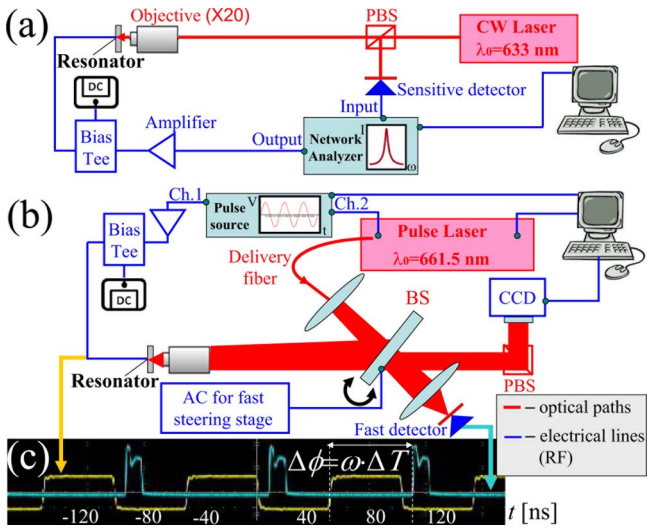

Fig. 1. (Color online) Experimental setup to study electromechanical resonators. (a) Frequency-domain arm, consisting of a sweeping rf network analyzer and a cw optical return loop. (b) Time-domain synchronous imaging arm. (c) Typical temporal traces of electrical drive (50% duty) and imaging beam pulses (10% duty).

sensitive identification of steady-state resonant modes. Modes in the range 40 kHz–3 GHz can be observed, as limited by the analyzer.

In the synchronous imaging arm [Fig. 1(b)], a pulse laser diode beam (Toptica iPulse, $\lambda_0 = 661.5$ nm) is used for resonator visualization. Direct electrical modulation with nanosecond gating times and minimum optical distortion is possible in the spectral range 0–500 MHz. The beam is collimated and illuminates the resonator through the reflection from a beam splitter (BS). The same objective is used for full-aperture illumination of the resonator. The frequency is set at a resonant mode (known from the FDS arm measurement) and all drives are supplied through the outputs of a phase-locked dual channel electrical pulse source producing unipolar square waves. One channel is used for the drive, with a duty cycle of 50%. The second channel triggers the imaging beam with narrow pulses of duty cycle 10% [Fig. 1(c) shows a typical oscilloscope trace of the drive and imaging pulse trains]. This provides an effective temporal window of $0.1T$, where T is the period. The stationary phase difference $\Delta\phi$ is scanned and corresponds to the intercycle sampling time ΔT. The BS is mounted on a fast steering stage to average the arbitrary speckle patterns, which are typically observed when collimated laser beams are used in nonuniform surface imaging. The backreflected signal is focused on a 3-megapixel CCD camera at the objective imaging plane. Direct optical synchronization obviates scanning mechanical stages, except for the above-mentioned steering BS. The high peak powers available (110 mW at the delivery fiber output without modulation) are crucial for sufficient back-reflection imaging signal, as substantial power losses are experienced at the BS interfaces. Higher duty cycle levels increase the power available for imaging on account of reduced temporal resolutions.

As a proof of principle, we analyze a circularly symmetric polycrystalline-Si (polySi, $n = 3.8$) microdrum resonator (disk-shaped film of diameter 25 μm and thickness 330 nm, suspended over an air gap on top of a Si wafer, with the latter serving as an actuation electrode; see [15,16]). An orifice (etch hole) of 4 μm diameter is present at the drum center. Figure 2(a) shows an FDS spectrum [using arm Fig. 1(a)] of the drum, under a 2 dBm (280 mV) ac excitation and 22 V dc bias. Mostly the first radially symmetric modes [(0,1) and (0,2), indexed by the number of nodes in the (circumferential, radial) directions] are efficiently excited. Synchronous images [arm Fig. 1(b)] at different times within a cycle, $0 < \Delta\phi < 360°$, are shown for the fundamental (0,1) and second symmetric (0,2) modes in Figs. 2(b) and 2(c), respectively. All differential interference images in Fig. 2 are obtained with respect to the reference image (bottom left of Fig. 2, full contrast) in the absence of ac electromechanical drive. Each image is subtracted from the reference and normalized by it. The modal patterns are observed in real time as a function of phase through the stationary image at the camera. As suggested by the contrast variations, in this resonator, the actuation regime is close to a fringe minimum at the imaging wavelength.

To extract from the measured optical images the actual mechanical mode shapes and device equilibrium suspen-

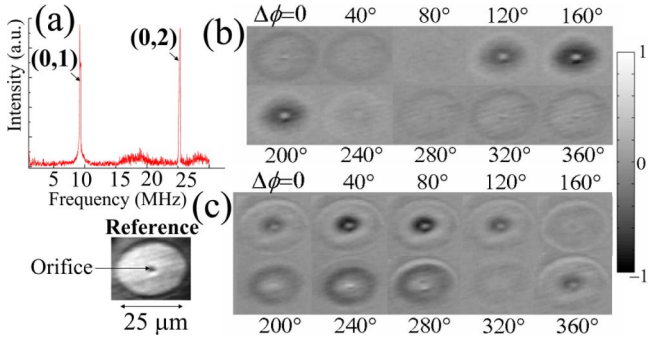

Fig. 2. (Color online) Drum resonator modes. (a) FDS spectrum. (b), (c) Synchronous imaging within a single cycle for: (b) fundamental mode (0,1), $f_0 = 9.2$ MHz and (c) second symmetric mode (0,2), $f_0 = 25.5$ MHz. All interference images are subtracted from the full contrast reference image of the drum (bottom left) and normalized.

sions, we use a Fabry–Perot interference analysis of the temporal traces. Figure 3(a) illustrates the cross section of our resonator, consisting of three dielectric layers (polySi, air gap, and thick single-crystal Si substrate), and definitions of model parameters. We write the air gap displacement as $d_1(x,t) = d_0 + A\cos(\omega t + \phi_0)$, where (A, d_0, ϕ_0) are the fitting parameters, ω is the drive frequency (assuming a linear response), and t is the time. At each in-plane radial point x, $A(x)$ corresponds to the vibration amplitude, $d_0(x)$ to the air gap elevation, and $\phi_0(x)$ to the phase between electrical drive and optical sampling pulses. Using a multilayer film interference analysis [17] and assuming normal incidence, the reflection coefficient is computed from

$$\begin{pmatrix} a \\ b \end{pmatrix} = M_{\text{tot}} \begin{pmatrix} 1 \\ n_s \end{pmatrix},$$

where a and b are scalars, $M_{\text{tot}} = M_2 M_1(t)$ is the composite transfer matrix [17], and n_s is the substrate refractive index. The corresponding reflectance is then $R = |\frac{a-b}{a+b}|^2$. The measured differential intensity is

$$I_{\text{diff}}(x,t) = R\{x, d_1(t)\} - R\{x, d_0\} \qquad (1)$$

A fit [Eq. (1)] is performed independently in each point x on a radial cross section [inset of Fig. 3(a)]. The mode profiles extracted for this section are shown for the (0,1) and (0,2) modes in Figs. 3(b) and 3(c), respectively. The equilibrium elevation profile $d(x)$ extracted from the first mode data is shown in Fig. 3(d). All profiles in the drum region converge within a small number of iterations and mostly yield smooth, low-error profiles along the drum section.

Numerical finite-element simulations [18] of the resonator modes, using a circumferentially clamped 25 μm circular drum with a concentric hole of 4 μm diameter, 190 nm elevation of the center above the clamped ends, and a cross-section geometry as in Fig. 3(a), reveal good correspondence with the experimental results in terms of the mode profiles [hollow circles in Fig. 3] and the fundamental mode frequency [Fig. 2(a)]. Small deviations of the measured profile shapes and mode frequencies from the ideal numerical values are estimated to result from presence of residual stress in the film, dc-bias-induced

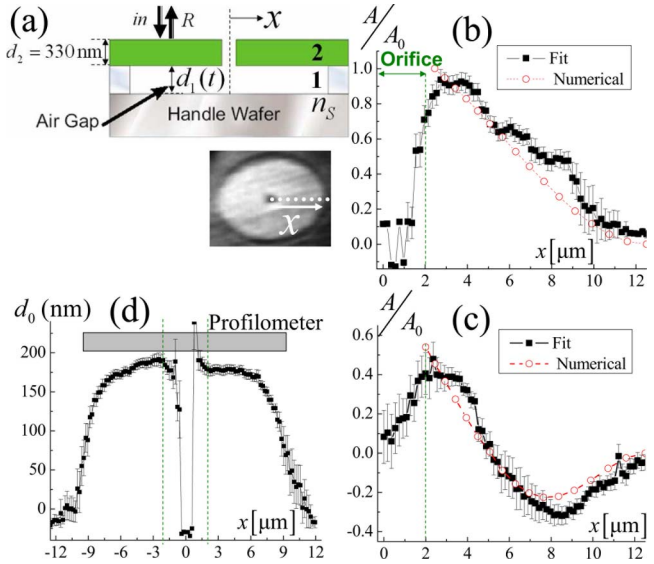

Fig. 3. (Color online) (a) Cross-section geometry used in the analysis. (b), (c) Mode profiles [estimated along the dashed line in the inset of (a)] for the first (0,1) and second (0,2) modes, respectively. (d) Equilibrium profile (d_0) estimated from the first mode fit. Hollow circles indicate numerical profile estimations. Error bars in the data indicate fit boundaries within a 95% confidence level around the average values.

nonlinear interactions, and device imperfections. Independent profilometry characterization around the orifice region (without vacuum or actuation) yielded a thickness of 200–225 nm for the air gap [gray area in Fig. 3(d)], in agreement with our all-optical estimation for d_0 near the drum center.

The sensitivity of amplitude detection deduced from Figs. 3(b) and 3(c) is 10%–30% of the peak amplitude. The total time required for an automated acquisition and averaging of dynamic mode shapes [such as in Figs. 2(b) and 2(c)] is ~1 min, and a subsequent fit procedure to each cross section [Figs. 3(b) and 3(d)] requires a processing time of ~4 min on a standard computer, offering rapid and robust electromechanical mode visualization and characterization.

This research was supported by the National Science Foundation (NSF) through grants DMR-0908634 and DMR-0520404.

References

1. H. G. Craighead, Science **290**, 1532 (2000).
2. M. Roukes, Phys. World **14**, 25 (2001).
3. K. L. Ekinci and M. L. Roukes, Rev. Sci. Instrum. **76**, 061101 (2005).
4. C. Ke and H. D. Espinosa, Small **2**, 1484 (2006).
5. D. Garcia-Sanchez, A. San Paulo, M. J. Esplandiu, F. Perez-Murano, L. Forr, A. Aguasca, and A. Bachtold, Phys. Rev. Lett. **99**, 085501 (2007).
6. B. Ilic, S. Krylov, L. M. Bellan, and H. G. Craighead, J. Appl. Phys. **101**, 044308 (2007).
7. J. V. Knuuttila, P. T. Tikka, and M. M. Salomaa, Opt. Lett. **25**, 613 (2000).
8. S. Petitgrand, R. Yahiaoui, K. Danaie, A. Bosseboeuf, and J. P. Gilles, Opt. Laser Eng. **36**, 77 (2001).
9. G. G. Fattinger and P. T. Tikka, Appl. Phys. Lett. **79**, 290 (2001).
10. H. Martinussen, A. Aksnes, and H. E. Engan, Opt. Express **15**, 11370 (2007).
11. K. Kokkonen and M. Kaivola, Appl. Phys. Lett. **92**, 063502 (2008).
12. C. Rembe and R. S. Muller, J. Microelectromech. Syst. **11**, 479 (2002).
13. P. Castellini, M. Martarelli, and E. P. Tomasini, Mech. Syst. Signal Process. **20**, 1265 (2006).
14. D. W. Carr and H. G. Craighead, J. Vac. Sci. Technol. B **15**, 2760 (1997).
15. M. Zalalutdinov, K. L. Aubin, M. Pandey, A. T. Zehnder, R. H. Rand, H. G. Craighead, J. M. Parpia, and B. H. Houston, Appl. Phys. Lett. **83**, 3281 (2003).
16. D. R. Southworth, H. G. Craighead, and J. M. Parpia, Appl. Phys. Lett. **94**, 213506 (2009).
17. M. Bass, *Handbook of Optics* (McGraw-Hill, 1995).
18. K. J. Bathe, *Automatic Dynamic Incremental Nonlinear Analysis* (ADINA R&D, Inc., 2005).